Journal of Geophysical Research: Atmospheres

RESEARCH ARTICLE
10.1029/2018JD028886

Key Points:
- A novel dew point depression method is presented for the calculation of fog-top height from radiosonde profiles
- Temperature inversions are 100-m deeper and twice as strong under fog conditions compared to nonfog conditions
- Arctic sea fog over coastal east Greenland is often several hundred meters thick

Correspondence to:
G. F. Gilson,
gaelle.gilson@uleth.ca

Citation:
Gilson, G. F., Jiskoot, H., Cassano, J. J., & Nielsen, T. R. (2018). Radiosonde-derived temperature inversions and their association with fog over 37 melt seasons in East Greenland. *Journal of Geophysical Research: Atmospheres*, *123*, 9571–9588. https://doi.org/10.1029/2018JD028886

Received 26 APR 2018
Accepted 4 AUG 2018
Accepted article online 15 AUG 2018
Published online 3 SEP 2018

Author Contributions:
Conceptualization: Gaëlle F. Gilson, Hester Jiskoot
Data curation: Gaëlle F. Gilson, Hester Jiskoot
Formal analysis: Gaëlle F. Gilson, Tyrell R. Nielsen
Funding acquisition: Gaëlle F. Gilson, Hester Jiskoot
Investigation: Gaëlle F. Gilson, Hester Jiskoot, John J. Cassano
Methodology: Gaëlle F. Gilson, Hester Jiskoot, John J. Cassano, Tyrell R. Nielsen
Resources: Hester Jiskoot
Supervision: Hester Jiskoot
Validation: Gaëlle F. Gilson
Visualization: Gaëlle F. Gilson
Writing - original draft: Gaëlle F. Gilson, Hester Jiskoot, Tyrell R. Nielsen

©2018. American Geophysical Union. All Rights Reserved.

Radiosonde-Derived Temperature Inversions and Their Association With Fog Over 37 Melt Seasons in East Greenland

Gaëlle F. Gilson[1], Hester Jiskoot[1], John J. Cassano[2], and Tyrell R. Nielsen[1]

[1]Department of Geography, University of Lethbridge, Lethbridge, Alberta, Canada, [2]Cooperative Institute for Research in Environmental Sciences and Department of Atmospheric and Oceanic Sciences, University of Colorado Boulder, Boulder, CO, USA

Abstract We present temperature inversion characteristics during fog and nonfog conditions at three east Greenland coastal weather stations during Arctic melt seasons 1980–2016. For this purpose, we developed a novel automated method to extract fog-top height (FTH) from Integrated Global Radiosonde Archive data, which is applicable to any fog thermodynamic profile and includes an improved interpolation of saturation between sounding levels. From the analysis of >22,000 melt-season soundings we conclude that inversions occur 85–95% of the time, are predominantly elevated, and have median depths >200 m. Fog at high-Arctic locations often penetrates the inversion layer, especially in the late melt season, and is commonly several hundred meters thick. At low-Arctic locations fog is thinner and generally restricted to the mixed layer. Inversions during fog are deeper and stronger compared to nonfog conditions. This effect is more pronounced at higher latitudes, which we attribute to distinct local boundary layer conditions and large-scale processes. The Integrated Global Radiosonde Archive-extracted FTHs have a cumulative error of 56 m and are in reasonable agreement with retrievals from Cloud-Aerosol Lidar and Infrared Pathfinder Satellite Observation satellite cloud top data. The novel FTH extraction method can be applied to any polar sounding with >5 significant levels below 700 hPa and can be extended to boundary layer clouds other than fog, which represent the majority of cloud occurrence in the Arctic melt season. This study advances the understanding of interactions between low clouds and temperature inversions and improves retrieval of cloud geometrical thickness from radiosondes: both have important implications for the Arctic surface energy budget.

Plain Language Summary Understanding how air temperature changes with height is important for weather forecasting and climate prediction. Usually air becomes colder as it rises in the atmosphere, except during temperature inversions when air near the ground is coldest. Inversions are common in polar regions, where they often occur together with fog during summer. Fog is a cloud at the Earth surface and influences temperature inversions by modifying air temperature and the amount of solar energy reaching the Earth surface. Up until now we did not have an adequate method to calculate fog thickness from weather balloon measurements (radiosondes). In this study we present an innovative method to calculate fog-top height using >22,000 summer radiosonde measurements taken at three stations in east Greenland from 1980 to 2016. Temperature inversions are almost always present, more than 200 m in vertical depth, and their base often starts more than 100 m above the ground. Fog is commonly 75- to 250-m deep and often penetrates the inversion layer. Temperature inversions during fog are deeper and have a larger temperature difference between top and base compared to nonfog conditions. We tested our method using independent techniques and recommend that it can be applied to most radiosonde measurements worldwide.

1. Introduction

The Arctic region is particularly sensitive to climate change and is in turn important for the global climate system (AMAP, 2017; Ford & Furgal, 2009; Intergovernmental Panel on Climate Change, 2013; Serreze et al., 2007). High northern latitudes have been warming at more than twice the rate of the rest of the planet, which is an accelerating phenomenon coined the Arctic amplification (Serreze & Francis, 2006). Arctic amplification is governed by positive feedback mechanisms such as albedo, lapse rate, water vapor, and cloud forcing and feedbacks (AMAP, 2017; Pithan & Mauritsen, 2014; Screen & Simmonds, 2010; Serreze & Barry, 2011; Taylor et al., 2013). Because of the complex interactions between these mechanisms and their spatial and

seasonal variability, the representation of the Arctic climate system in regional and global climate models requires improvement (Bintanja & Krikken, 2016; Flato et al., 2013; Kattsov & Källén, 2005). The main aim of this paper is to provide measurements and improve understanding of the interaction between two phenomena influencing these feedback mechanisms: temperature inversions and fog. Near-surface temperature lapse rates, low cloud thermodynamic structure, and their interactions play a key role in the surface energy balance. Although several studies have increased our understanding of the interactions between low-level clouds and inversion characteristics during the Arctic melt season, interactions between fog and temperature inversions have not been fully explored (e.g., Devasthale et al., 2010; Kahl et al., 1992; Mernild & Liston, 2010; Sedlar & Tjernström, 2009; Sedlar et al., 2012).

Low-level temperature inversions (i.e., increase of temperature with altitude; Oke, 1987) are frequent year round in the Arctic but dominant in winter (Bintanja et al., 2011; Devasthale et al., 2010; Marshall et al., 2007; Serreze et al., 1992). Inversions can have complex effects on the Arctic surface energy budget, depending on their structure, coincidence with clouds, and seasonality. Wintertime inversions intensify Arctic amplification, because the ability of the clear-sky atmosphere to cool to space decreases with inversion strength. (Bintanja et al., 2011; Lesins et al., 2012). Summertime inversions can have contrasting temperature and radiative effects and have been observed to reduce glacier ablation as well as cause episodes of intense sea ice melt (Chutko & Lamoureux, 2009; Mernild & Liston, 2010). In the Arctic melt season, inversions with an elevated base are most common over the Arctic Ocean and coastal areas (Kahl, 1990; Kahl et al., 1992, 1996) and mainly originate from subsidence or advection processes (Busch et al., 1982). Surface-based inversions can also occur and usually result from ice and snow melt (Kahl et al., 1992; Miller et al., 2013). Surface turbulence, precipitation, topography, warm-air advection, and the presence of low-level clouds and fog can all influence temperature inversion characteristics (Bourne et al., 2010; Bradley et al., 1992; Hudson & Brandt, 2005; Kahl, 1990; Mernild & Liston, 2010; Miller et al., 2013; Serreze et al., 1992). Of these, the interaction between inversions and low-level clouds is the least studied.

Low stratiform clouds are the most common cloud type during the Arctic melt season and significantly influence the surface energy budget (Curry et al., 2000; Eastman & Warren, 2010; Klein & Hartmann, 1993). Among these clouds, Arctic sea fog (visibility lower than 1 km, National Oceanic and Atmospheric Administration, 1995) occurs often (Alt, 1979; Hanesiak & Wang, 2005; Nilsson & Bigg, 1996; Rae, 1951; Sotiropoulou et al., 2016; Svendsen et al., 2002). Sea breeze may advect fog onto coastal areas, where it becomes capped by warm continental air, creating strong stability conditions (Alt, 1979; Cappelen, 2015; Lewis et al., 2003; Mernild et al., 2008). The high reflectivity of low clouds and fog cools the surface while their emissivity warms the surface. The net effect is usually a warming of the surface, although this depends on the droplet size, liquid water path, surface albedo, and the solar zenith angle (Mauritsen et al., 2011; Nardino & Georgiadis, 2003; Shupe & Intrieri, 2004). Over the Greenland ice sheet, liquid-bearing low-level clouds are attributed to enhance mass loss over the accumulation zone (Bennartz et al., 2013; Miller et al., 2015; Van Tricht et al., 2016), while over low-albedo zones of the ablation area they may suppress melt (Hofer et al., 2017; Wang et al., 2016).

The Integrated Global Radiosonde Archive (IGRA, Durre et al., 2006) has been widely used to study temperature inversions in the Arctic (e.g., Bradley et al., 1992; Chutko & Lamoureux, 2009; Fochesatto, 2015; Kahl, 1990; Serreze et al., 1992; Zhang et al., 2011). While IGRA-derived temperature and humidity profiles have been used to study Arctic low-level stratiform cloud and fog macrophysical structure (e.g., Dorman et al., 2017; Nygård et al., 2014), the thermodynamic structure of these clouds has mostly been investigated from ship campaign measurements (Sedlar et al., 2012; Sedlar & Tjernström, 2009; Shupe et al., 2013; Sotiropoulou et al., 2014) and only recently from archived radiosonde observations (Gilson et al., 2018). Two fog-top retrieval techniques from temperature profiles have been documented to date: the mixing ratio method (MRM, Bauer & Howlett, 1995) and the temperature convergence method (TCM; e.g., Román-Cascón et al., 2015). The MRM uses the intersection of the average mixing ratio between the bottom and top of the inversion with the dry-bulb temperature curve to calculate fog-top height (FTH) and is presented for application to radiation fog with a surface-based inversion (Bauer & Howlett, 1995). The MRM has not been applied to sea fog or fog with an elevated inversion, both of which frequently occur during the Arctic melt season (Kahl, 1990; Kahl et al., 1992; Serreze et al., 1992). In the TCM, fog top is estimated from the height of the capping inversion or from the first layer where the thermal profile is near neutral or unstable. The TCM cannot be applied to shallow fog or fog with a surface-based inversion and, in addition, requires either high vertical-

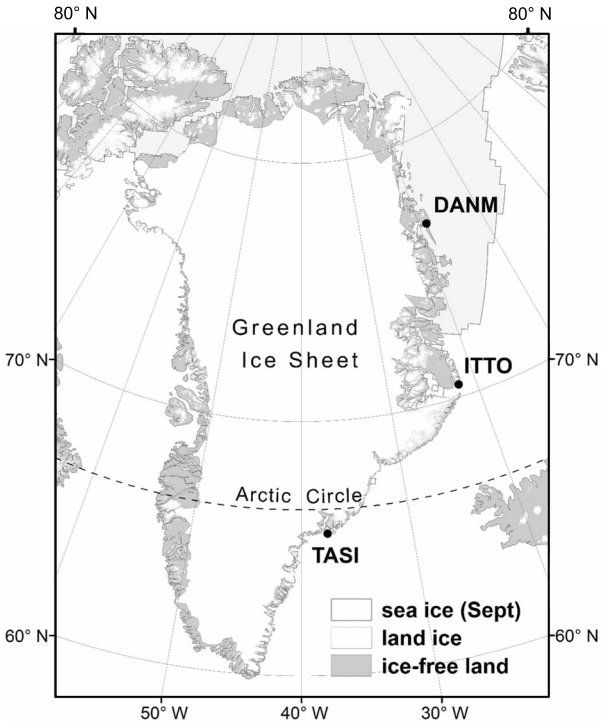

Figure 1. Location of radiosonde stations along the coast of east Greenland: Danmarkshavn (DANM), Ittoqqortoormiit (ITTO), and Tasiilaq (TASI). The September sea-ice extent represents the median minimum seasonal extent (http://nsidc.org/data/nsidc-0051). Land ice extent is mapped by combining the Randolph Glacier Inventory (Pfeffer et al., 2014) with the hydrologic outlets of the Greenland ice sheet (Lewis & Smith, 2009).

resolution or high temporal-resolution profiles (Román-Cascón et al., 2015). Several other techniques have been proposed to retrieve cloud base, top, and thickness from low- and high-resolution radiosonde profiles (e.g., Chernykh & Eskridge, 1996; Minnis et al., 2005; Poore et al., 1995; Wang & Rossow, 1995; Zhang et al., 2010, 2013). These techniques use dew point depression thresholds or variations in relative humidity (RH) but disregard fog and do not perform well over Arctic locations (Jin et al., 2007; Zhang et al., 2013). Development of a cloud top height detection method from radiosondes for Arctic fog or low stratiform clouds specifically would therefore fill an important scientific gap.

In this paper, we quantify lower tropospheric inversion characteristics during fog and nonfog weather conditions in the Arctic. To achieve this goal, a novel dew point depression method (DDM) to retrieve FTH from IGRA low-resolution radiosonde observations is introduced and applied to the period 1980–2016 at three east Greenland synoptic weather station locations with fog observations. Verification of our results and methods used include (i) a sensitivity analysis of the dew point depression threshold, (ii) a comparison of the DDM to the established MRM (Bauer & Howlett, 1995), and (iii) a comparison of IGRA cloud top and fog-top retrievals to those from collocated Cloud-Aerosol Lidar and Infrared Pathfinder Satellite Observation (CALIPSO).

2. Study Site

Three radiosonde stations associated with World Meteorological Organization (WMO) synoptic weather stations were selected along the east coast of Greenland (Figure 1), where fog is most prevalent in summer (Cappelen, 2015). These stations are operated by the Danish Meteorological Institute (DMI) and are part of the IGRA (network portal: https://www.ncdc.noaa.gov/data-access/weather-balloon/integrated-global-radiosonde-archive, Durre et al., 2006). The climate zone type ranges from low Arctic, with seasonal sea ice and a strong diurnal solar cycle (Tasiilaq: WMO ID 4360, 54 m above sea level, asl, 65.61°N, 37.64°W), to high Arctic, with year-round sea ice concentrations above 80%, 24-hr daylight, and a dominance of low clouds and fog (Ittoqqortoormiit: WMO ID 4339, 70 m asl, 70.48°N, 21.95°W; Danmarkshavn: WMO ID 4320, 11 m asl, 76.77°N, 18.67°W) (Cappelen et al., 2001; Circumpolar Arctic Vegetation Map, 2003; Vinje, 2001). The climate at Tasiilaq is strongly influenced by the presence of the Icelandic Low and the warm Irminger Current as well as the passage of cyclones, which generally result in optically thicker clouds compared to more northern locations (Cappelen, 2015; Hanna & Cappelen, 2003; Van Tricht et al., 2016).

3. Data and Methodology

3.1. Temperature Inversions

3.1.1. Upper-Air Observations From IGRA Radiosonde Data

The analysis of radiosonde data in this work is restricted to the period 1980–2016 in order to remove data inhomogeneity due to major changes in sonde type, radiation correction, and station relocations (Antikainen et al., 2002; Durre & Yin, 2008). In addition, only the Arctic melt season months of May to August are considered (hereafter referred to as *summer*), when two thirds to three quarters of annual fog occurs in east Greenland (Cappelen et al., 2001; Gueye, 2014). Radiosonde data were acquired through the quality-controlled IGRA network. Launch times were either at 1100 and 2300 UTC or at 1200 and 0000 UTC. Each radiosonde records temperature, humidity, atmospheric pressure, and wind speed and direction. Soundings contain data at mandatory pressure levels (1000, 925, 850, 700, 500 hPa, etc.) and at additional significant thermodynamic levels capturing all slope breaks in temperature and humidity profiles between mandatory levels (Durre et al., 2006). We restrict our data analysis to below the 700-hPa pressure level or approximately below 3,000 m asl. Between 1980 and 2016 there has been an alternate use of Vaisala sonde types RS18/21 (until early 1980s), RS80, RS90, and RS92, which have an accuracy of 1 hPa-, 0.5 K-, 5% RH-, and

25-m derived resolution for calculated geopotential height (Vaisala, 2017). We did not apply a correction for the temperature sensor response time, but given a response time of <0.4 s and a balloon ascent rate of 5 m s^{-1} (Vaisala, 2017), the error in calculated height due to the response time is always <2 m, which is an order of magnitude smaller than the uncertainty in derived measurements of geopotential height.

3.1.2. Radiosonde Analysis Methodology

IGRA variables used for the analysis of temperature inversions include dry-bulb temperature (T in kelvin, converted to degree Celsius), atmospheric pressure (P in hectopascal), and geopotential height that is only reported at mandatory pressure levels (Z in meter). IGRA computes the thickness of the layer ΔZ_L between level i of reported Z and level $i+1$ of unknown Z via the hydrostatic balance formula, which requires knowledge of T and P at levels i and $i+1$:

$$\Delta Z_L = \frac{R}{g}\left(\frac{T_i + T_{i+1}}{2}\right)\ln\frac{P_i}{P_{i+1}}, \tag{1}$$

where R is the ideal gas constant (287 $J{\cdot}K^{-1}{\cdot}kg^{-1}$) and g is the gravitational acceleration (9.81 m s^{-2}, Durre & Yin, 2008). Throughout this analysis calculated Z will be used only. Surface wind speed (w_s in meter per second) at the first sounding level will be used to analyze its effect on inversion characteristics. Soundings with fewer than five levels below the 700-hPa level in T profiles are discarded, as these are considered unreliable for the analysis of low tropospheric inversions (Kahl et al., 1992).

Low tropospheric temperature inversions are characterized on the basis of their base height (Z_{base}), top height (Z_{top}), depth (ΔZ), and intensity (ΔT) using the method from Kahl (1990). Z_{base} is determined as the first level where T starts to increase with height. The inversion is classified as a surface-based inversion when Z_{base} is at ground level and as a low-level inversion when Z_{base} is elevated but below the 700-hPa pressure level (Kahl et al., 1992). Z_{top} is the altitude above the ground level at which T starts to decrease with height above Z_{base}. As recommended by Kahl (1990) and Zhang and Seidel (2011), thin layers (< 100 m) of positive temperature lapse rates between two inversion layers are considered to be part of the same inversion layer. Multilayered inversions in high vertical resolution profiles could be calculated using methods from Fochesatto (2015), but these were not applied here. Ultimately, ΔZ is obtained by subtracting Z_{base} from Z_{top}, and ΔT is calculated as the difference in T between Z_{top} and Z_{base}.

3.2. Fog, Cloud Cover, and Wind

3.2.1. Surface Observations of Fog and Cloud Cover From Synoptic Weather Stations

Fog conditions are extracted from a combination of archived present weather (*ww*) and visibility (*vv*) data provided by DMI for the three WMO synoptic weather stations. Manual observations were made every 3 hr starting at 0000 UTC until the early 2000s, when observations became automated and reported hourly (Bødtker, 2003). The manual and automated *ww* and *vv* fog and visibility codes used here are from tables 4677, 4680, 0, 20, 003, and 4377 of World Meteorological Organization (1995). Automated *ww* and *vv* observations are currently reported using a forward scatter FD12P Vaisala Present Weather Sensor, with a Meteorological Optical Range accuracy of ±10% (C. Nehring, personal communication, 2016). We restrict our analysis to summer liquid or supercooled fog (surface T from radiosondes > −10 °C: Petterssen, 1956), which represents >95% of summer fog observations in this region (Gilson, 2018).

For the analysis of the general effects of clouds other than fog on temperature inversion characteristics, we use DMI cloud cover fraction data (Cappelen, 2015). We distinguish three cloud cover categories: (1) clear-sky conditions (0 okta), (2) few and scattered clouds (1–4 oktas), and (3) broken and overcast conditions (5–8 oktas). Neither cloud type nor cloud altitude is available from DMI files, but given that low-level clouds are dominant in Arctic coastal regions in summer (Eastman & Warren, 2010; Key et al., 2004; Klein & Hartmann, 1993) we assume that cloud cover fraction, especially when broken to overcast, is mainly representative of low-level cloud conditions.

3.2.2. FTH Calculation From IGRA Soundings

From all IGRA summer soundings over the period 1980–2016, profiles coincident with fog were retrieved based on the combined analysis of synoptic fog observations (*ww* and *vv*) from DMI archived data and the dew point depression (T_{dd}) data available in IGRA files. Soundings with fewer than five levels in T_{dd} profiles below the 700-hPa level were excluded. Because of the combined use of manned and automated synoptic *ww* and *vv* observations in this analysis, some soundings correspond to ground observations (0000 UTC

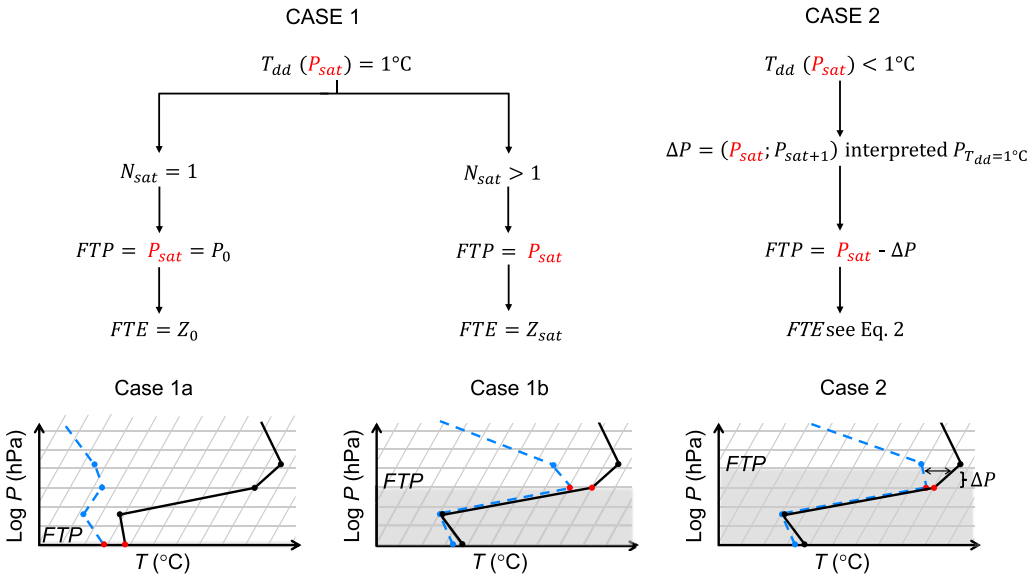

Figure 2. Dew point depression method (DDM) of determining fog-top pressure (FTP) and fog-top height (FTH) from dew point depression T_{dd} on a schematic Skew-*T* Log-*P* diagram. The solid black curve is the dry-bulb temperature *T*, and the dashed blue curve is the dew point temperature ($T_d = T - T_{dd}$). The uppermost saturated pressure level P_{sat} (red dot) corresponds to a geopotential height Z_{sat} and is determined as the uppermost level above a continuous saturated layer (gray shading) where $T_{dd} \leq 1$ °C. FTP is the level where $T_{dd} = 1$ °C. N_{sat} is the number of saturated levels between the surface pressure P_0 and P_{sat}.

and 1200 UTC: soundings before automation and all soundings after automation) while others do not (1100 UTC and 2300 UTC: soundings before automation).

Based on T_{dd}, *ww*, *vv*, and the time lag between ground and upper-air observations, three sounding categories, including two categories of fog (*fog conditions*), were defined for this analysis.

1. *Real fog*: soundings corresponding to synoptic fog observations at the station with *vv* < 1 km or occurring at sounding times between two consecutive synoptic fog observations at the station with *vv* < 1 km. Real-fog soundings were additionally restricted to a surface dew point depression of $T_{dds} \leq 1$ °C, a common value for saturation of advection fog (Koračin et al., 2014). This restriction captures almost all synoptic real-fog observations at Tasiilaq and Danmarkshavn and about 75% of fog observations at Ittoqqortoormiit (Gilson et al., 2018, Figure 2). By extension, *saturation* will be defined in this paper as $T_{dd} \leq 1$ °C. It corresponds to a RH with respect to water >93% (Hardy, 1998).
2. *Marginal fog*: soundings corresponding to *ww* codes of fog in patches, fog from a distance, shallow fog <2 m above ground level (agl, cf. Croft et al., 1997), or, in the case of soundings not coincident with synoptic observations, real fog either immediately before or after the balloon launch, but not both. For marginal fog no threshold was set for T_{dds} or *vv* given the thin, patchy, or noncontinuous nature of the fog that suggests that the radiosonde data may not coincide with the fog occurrence in either time or space.
3. *Nonfog*: soundings during all other weather conditions during summer.

For both real and marginal fog, soundings that were not coincident in time with synoptic fog observations represented 50–70% of analyzed upper-air observations over the study period (1980–2016).

Fog-top pressure (FTP) and FTH for real fog were computed with a method based on IGRA's T_{dd} profiles, which will hereafter be referred to as the DDM (see Figure 2). First, the pressure of the uppermost saturated sounding level (P_{sat}), with $T_{dd} \leq 1$ °C, corresponding to the geopotential height Z_{sat} is determined as the uppermost level above a continuous saturated layer (Figure 2, gray shading). FTP is the level where $T_{dd} = 1$ °C. T_{dd} at P_{sat} is either 1 °C (Cases 1a and 1b) or < 1 °C (Case 2). In Case 1a, P_{sat} is at ground level and $T_{dd} = 1$ °C. Here FTP is at the ground level, and FTH is the geopotential height at the ground level (Z_0). In Case 1b, P_{sat} is above the surface and $T_{dd} = 1$ °C. Here fog is delimited by at least two saturated sounding levels, and FTH corresponds to Z_{sat}. In Case 2, P_{sat} is elevated and $T_{dd} < 1$ °C. The pressure difference (ΔP)

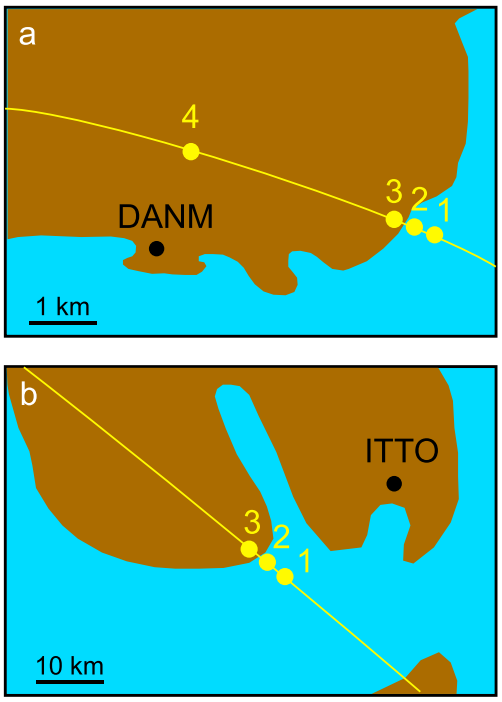

Figure 3. Schematic representation of selected grid points (yellow dots) from the optimal CALIPSO track line (yellow line) in the vicinity of (a) Danmarkshavn (DANM) and (b) Ittoqqortoormiit (ITTO). Grid points 1–3 are the nearest coastal locations on a CALIPSO track to each IGRA station (8 and 28 km, respectively). Grid point 4 in Figure 3a is the nearest CALIPSO point on land, 2 km north of Danmarkshavn. IGRA = Integrated Global Radiosonde Archive; CALIPSO = Cloud-Aerosol Lidar and Infrared Pathfinder Satellite Observation.

between P_{sat} and FTP is determined geometrically on the Skew-*T* Log-*P* diagram by linear interpolation at 0.1-hPa intervals between P_{sat} and the next subsaturated level aloft ($P_{sat\ +\ 1}$), until T_{dd} = 1 °C. In this case, FTH is the sum of Z_{sat} (from IGRA data files) and the calculated saturated thickness above that level, which is obtained from a modification of equation (1) under the assumption of hydrostatic balance and linear variation of T and T_d between two consecutive sounding levels. Thus, FTH for Case 2 is calculated as follows:

$$\mathrm{FTH} = Z_{sat} + \frac{R}{g}\left(\frac{T_{sat} + \mathrm{FTT}}{2}\right)\ln\frac{P_{sat}}{\mathrm{FTP}}, \tag{2}$$

where FTH and Z_{sat} are in m asl, R is 287 J·K^{-1}·kg^{-1}, g is 9.81 m s^{-2}, temperatures at P_{sat} (T_{sat}) and at the fog top (FTT) are in K, and P_{sat} and FTP are in hectopascal.

The DDM was used instead of the established MRM (Bauer & Howlett, 1995) because of the inability of the MRM to calculate FTH in cases of negative T_d gradients above one single saturated sounding level (FTH below Z_{base}). These occur in up to 57% of radiosonde profiles with fog over east Greenland (Gilson et al., 2018). A comparative analysis of the DMM and MRM is presented in section 5.1.

Inversion characteristics during fog conditions were calculated using the method explained in section 3.1.2 for all-weather cases, with one exception: when a secondary weak inversion was present inside a fog layer below the main capping inversion (occurring in <3% of soundings), the inversion characteristics of that capping inversion were retained. Z_{base}, ΔZ, and ΔT were analyzed for all real, marginal and nonfog soundings. In addition, for a better understanding of regional differences of inversion characteristics during fog conditions, statistics for Z_{base}, ΔZ, and ΔT were computed for two categories of wind speed ($<$ 5 and $\geq$ 5 m s^{-1}) for all-weather, real-fog, and nonfog conditions (see section 4.1.2). We statistically analyzed the significance of differences in Z_{base}, Z_{top}, ΔZ, and ΔT among all-weather, nonfog, and fog conditions, as well as the FTH among the three stations using the nonparametric Wilcoxon Rank Sum and the combined Kruskal-Wallis and Tukey's Honest Significant Difference tests at the 99% confidence level.

3.2.3. Fog and Low Clouds From CALIPSO

IGRA-derived FTH were compared to an independent cloud altitude data set from the CALIPSO Level 2 cloud layer product at 1 km along-track resolution (CAL_LID_L2_01kmCLay-Standard_V4–10 from https://www-calipso.larc.nasa.gov/). CALIPSO provides vertical profiles of aerosols and clouds with a vertical resolution of 30 m (Winker et al., 2009) and has been found to accurately capture fog frequency and spatial distribution when no upper clouds are present (Cermak, 2016; Kawai et al., 2015).

We selected CALIPSO tracks and times that coincide closest to the three radiosonde locations and launch times. For Tasiilaq the closest CALIPSO track timing is >3 hr earlier or later than its radiosonde launches, and we therefore exclude this station from our comparison. Danmarkshavn and Ittoqqortoormiit have the nearest CALIPSO track lines at 1230 UTC and 1330 UTC, respectively, which is approximately coincident with their 1200 UTC radiosonde balloon launches. For these two stations, three or four grid points on the nearest CALIPSO tracks (Figure 3) were selected to account for spatial variability in fog thickness. Although Danmarkshavn's nearest track line point is only 2 km north of the station (Figure 3a, point 4), the coastal mountainous topography can affect FTH, and we therefore also extracted the nearest three coastal grid points, approximately 8 km east of the station (Figure 3a, points 1–3). The nearest optimal track line to Ittoqqortoormiit passes 28 km to the southwest over the wide fjord Scoresby Sund, from which three coastal grid points were selected (Figure 3b, points 1–3). For each of the 16-day repeat tracks between April and October 2006–2016, all corresponding IGRA radiosonde profiles and DMI *ww* data were checked for fog occurrence so as to cover all liquid fog in the early to late melt season (cf. Gilson, 2018). Thin fog

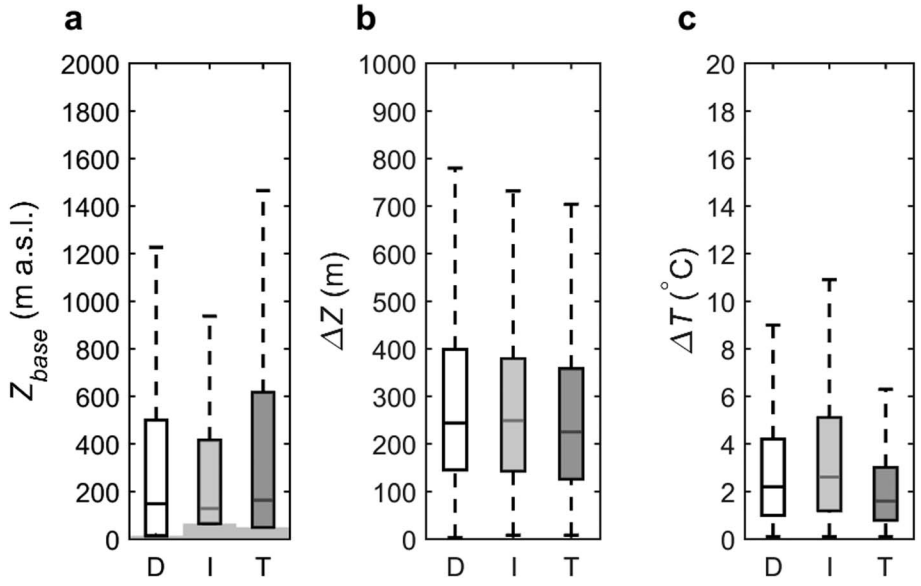

Figure 4. Inversion characteristics for summers of 1980–2016 during all-weather conditions for Danmarkshavn (D), Ittoqqortoormiit (I), and Tasiilaq (T). Box-and-whisker plots show the median (horizontal line), lower and upper quartiles (bottom and top of box), and 5th and 95th percentiles (range) for (a) inversion base (Z_{base}), with ground elevation (light gray shading below boxes), (b) inversion depth (ΔZ), and (c) inversion intensity (ΔT).

(FTH $<$ 100 m asl) was excluded due to its spatial and temporal variability. Since only four fog observations correspond to the CALIPSO timing, we expanded our comparison analysis to include cloud top heights from low stratiform clouds without precipitation. Fog and cloud top heights were extracted using the maximum altitude of the lowermost cloud level in the CALIPSO Level 2 cloud layer product.

4. Results and Interpretation

4.1. Temperature Inversion Characteristics

4.1.1. All-Weather Conditions

In total, 7,786 summer soundings were retrieved and analyzed for Tasiilaq, 7,271 for Danmarkshavn, and 7,453 for Ittoqqortoormiit. Lower tropospheric inversions occur in 84% of soundings at Tasiilaq, 91% of soundings at Danmarkshavn, and 95% of soundings at Ittoqqortoormiit. Most inversions are elevated, with frequencies ranging from 69% at Tasiilaq to 79% at Ittoqqortoormiit. Median inversion-base altitudes (Z_{base}) are highest at Tasiilaq (164 m asl) and lowest at Ittoqqortoormiit (129 m asl) compared to Danmarkshavn (149 m asl; $p < 10^{-3}$, Figure 4a). Median inversion depths (ΔZ) range from 225 to 249 m (Figure 4b) and are significantly lower over Tasiilaq compared to the other two stations ($p < 10^{-8}$). Inversion intensities (ΔT) are significantly different among all stations, with Ittoqqortoormiit and Tasiilaq exhibiting the highest (ΔT = 2.6 °C) and lowest (ΔT = 1.6 °C) median values, respectively (Figure 4c, $p < 10^{-9}$).

Over the period 1980–2016, no linear trend occurs in ΔT, but median Z_{base} decreased over Danmarkshavn and Ittoqqortoormiit by 98 and 115 m (adjusted R^2 = 0.17–0.22; $p < 0.01$) and median ΔZ decreased over all stations by 109–124 m (adjusted R^2 = 0.11–0.32; $p < 0.05$). Conversely, 1981–2015 summer ERA-Interim reanalysis data over Ittoqqortoormiit present a positive trend in surface-based inversion ΔT and no trend in surface-based inversion ΔZ (Palarz et al., 2018). Without homogenization of our IGRA data sets (e.g., Haimberger, 2007; Lanzante, 1996), which is beyond the scope of this paper, we cannot determine whether our apparent trends are due to actual changes in inversion characteristics or because of the gradual increase in significant sounding levels since 1980 (Antikainen et al., 2002; Durre & Yin, 2008; Gilson, 2018).

4.1.2. Fog Conditions

Real fog occurs with a lower tropospheric inversion over 99% of the time, with 84–86% of real-fog cases corresponding to low-level inversions. Inversion characteristics during real fog, marginal fog, and nonfog

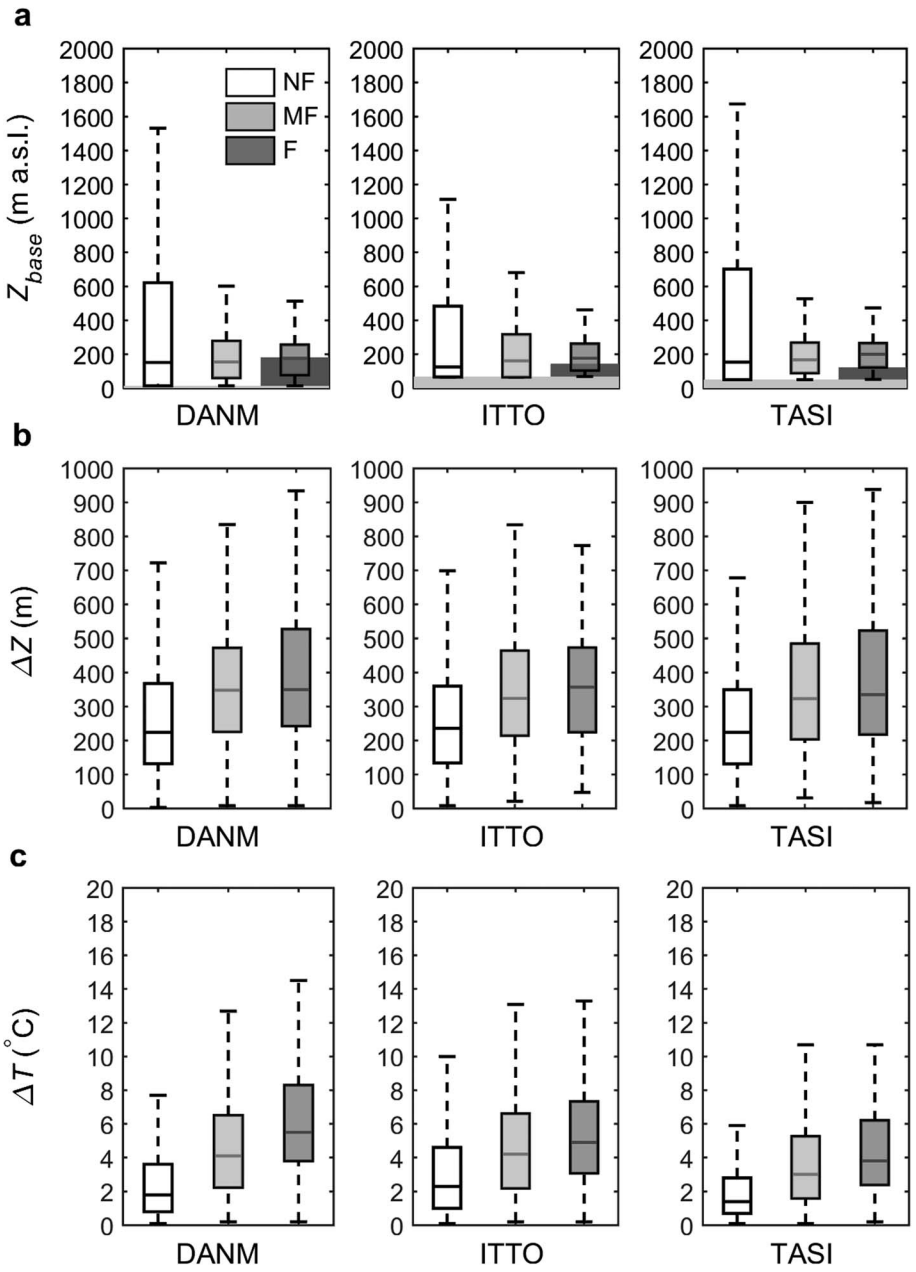

Figure 5. Inversion characteristics for summers of 1980–2016 during nonfog (NF), marginal fog (MF), and real-fog (F) conditions over Danmarkshavn (DANM), Ittoqqortoormiit (ITTO), and Tasiilaq (TASI). Box-and-whisker plots are for (a) inversion base (Z_{base}), with ground elevation (light gray shading below boxes) and median fog thickness above ground (dark gray shading, see section 4.2), (b) inversion depth (ΔZ), and (c) inversion intensity (ΔT).

conditions are shown in Figure 5. At each station these include about 150, 800, and 5,000 observations, for each fog condition, respectively. Median Z_{base} altitudes during real fog are at 176–200 m asl (Figure 5a). Even though they appear marginally higher under fog conditions, no significant difference transpires among real-fog, nonfog, or marginal fog conditions (p = 0.05–0.19), nor among stations. Median ΔZ during marginal and real fog are 335–357 m and similar at all stations, but inversions are deeper during fog conditions than during nonfog conditions (by 111–126 m on average, $p < 10^{-10}$, Figure 5b). At all stations inversions are stronger during real fog than during nonfog conditions (Figure 5c, $p < 10^{-9}$), but at Danmarkshavn and Tasiilaq they are also stronger than during marginal fog ($p < 10^{-2}$). During nonfog conditions, inversions are strongest at Ittoqqortoormiit (median = 2.3 °C, $p < 10^{-9}$) and weakest at Tasiilaq

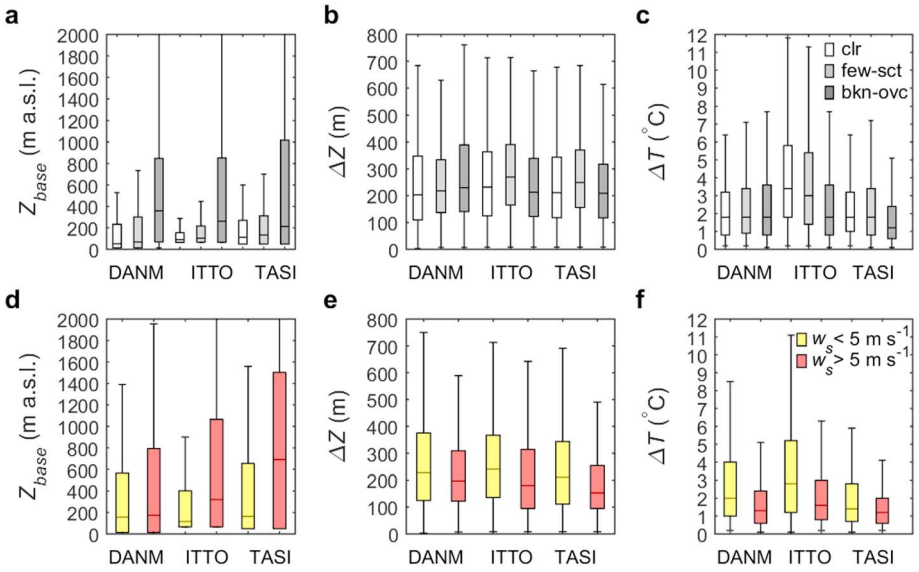

Figure 6. Box-and-whisker plots for inversion base (Z_{base}), inversion depth (ΔZ), and inversion intensity (ΔT) during nonfog weather conditions for (a–c) cloud cover classes (clr, clear sky; few-sct, few and scattered clouds; bkn-ovc, broken and overcast) and (d–f) wind speed categories (w_s). DANM = Danmarkshavn; ITTO = Ittoqqortoormiit; TASI = Tasiilaq.

(median = 1.4 °C, $p < 10^{-7}$). Under marginal fog conditions, inversions are weakest at Tasiilaq (median = 3 °C, $p < 10^{-7}$) but do not differ significantly between Ittoqqortoormiit and Danmarkshavn (medians = 4.1 and 4.2 °C, respectively, $p = 1$). Inversions are weaker during real-fog conditions at Tasiilaq than at Danmarkshavn (median ΔT = 3.8 °C versus 5.5 °C, $p < 10^{-5}$), while Ittoqqortoormiit is intermediate, though not significant (median ΔT = 4.9 °C, p range = 0.05–0.09). The largest differences in ΔT and ΔZ between fog and nonfog conditions occur at Danmarkshavn.

Inversion characteristics during nonfog conditions under different categories of wind speed (w_s) and cloud cover fraction are presented in Figure 6. These statistics include over 1,000 observations for all cloud and wind speed categories, except for $w_s > 5$ m s^{-1} at Tasiilaq where $n = 279$. Only results for nonfog conditions are shown because these results are nearly identical to those for all-weather conditions, and because fog in East Greenland typically occurs at $w_s < 5$ m s^{-1} (Gilson, 2018), and fog prevents observers from making cloud observations. At all stations, Z_{base} is the highest under broken-overcast conditions (Figure 6a, $p < 10^{-9}$). The median difference ranges from 100 to 306 m, with the highest inversion base at highest latitudes. At Ittoqqortoormiit and Tasiilaq inversions are weaker under cloudy conditions (median ΔT = 0.6 °C) than during clear-sky conditions (median ΔT = 1.6 °C, $p < 10^{-9}$), but this difference is not observed at Danmarkshavn (Figure 6c). Low w_s is associated with stronger (up to 1.2 °C on average, $p < 0.01$; Figure 6f) and deeper (30–61 m, $p < 10^{-5}$; Figure 6e) inversions over all stations. Increased w_s significantly elevates Z_{base} over Ittoqqortoormiit and Tasiilaq ($p < 10^{-6}$) but not over Danmarkshavn (Figure 6d). These conclusions remain unchanged when grouping w_s into three classes (< 5, 5–10, >10 m s^{-1}, not shown) instead of two. During fog, however, inversion characteristics do not differ between low or high w_s conditions (not shown). Biases in this statistical analysis may exist due to the unequal sample sizes between the two distributions because w_s above 5 m s^{-1} is not common during fog.

4.2. FTH and the Inversion Layer

Median summer-averaged FTH is at 123, 145, and 182 m asl over Tasiilaq, Ittoqqortoormiit, and Danmarkshavn, respectively (Figure 7). Fog thickness (FTH minus station elevation) is significantly higher over Danmarkshavn ($p < 0.01$), but FTH does not differ from the other two stations. Danmarkshavn is characterized by significant differences between early (May–June) and late (July–August) melt season ($p = 0.0031$), with a median late melt season FTH at 220 m asl (not shown). At Danmarkshavn, median summer-averaged FTH extends slightly above the median Z_{base}; in the late melt season, fog penetrates the inversion layer by on

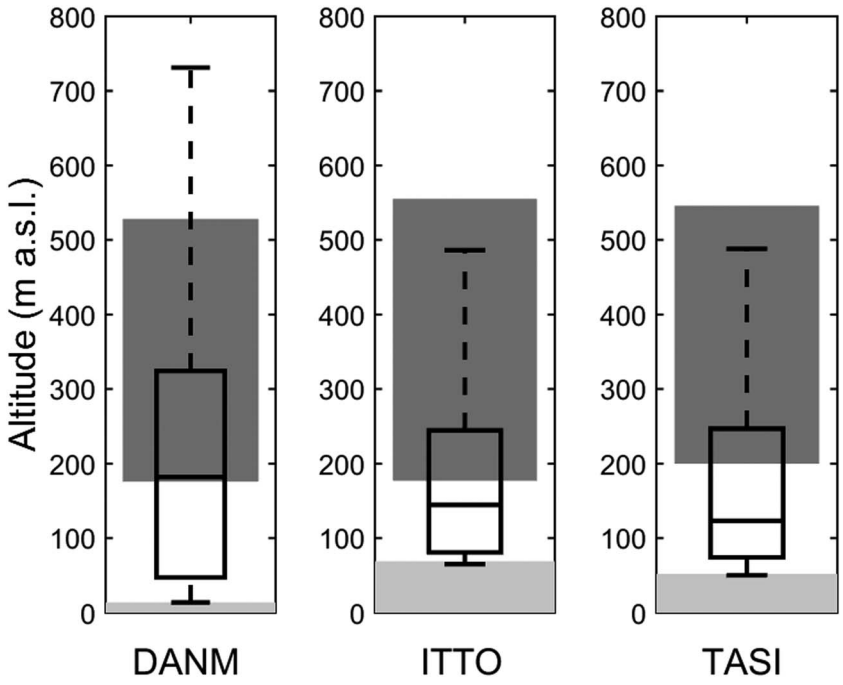

Figure 7. Fog-top height (box-and-whisker plots) and median inversion layer (dark gray shading) over Danmarkshavn (DANM, n = 175), Ittoqqortoormiit (ITTO, n = 105), and Tasiilaq (TASI, n = 111) for summers of 1980–2016. The light gray shading below the boxes is the ground elevation.

average 47 m. In contrast, the median FTH is below the median Z_{base} at Ittoqqortoormiit and Tasiilaq. This coincides with thermodynamic classification results presented in Gilson et al. (2018). There is no significant linear trend in FTH between 1980 and 2016.

5. Discussion

5.1. Sensitivity Analysis of FTH Calculation

The DDM for calculation of FTH presented in this paper uses a dew point depression (T_{dd}) threshold of 1 °C to determine air parcel saturation and the presence of fog. Even though this threshold is commonly reported for liquid fog over midlatitude locations (e.g., Kim & Yum, 2010; Koračin et al., 2014; Meyer & Rao, 1999), it is smaller than thresholds traditionally used for cloud detection at subzero temperatures (Poore et al., 1995). In this section we verify the FTH calculations through a comparison with the MRM (Bauer & Howlett, 1995) using a T_{dd} threshold of 1 ± 0.5 °C and through a sensitivity analysis using a range of T_{dd} threshold values between 0.5 and 1.5 °C.

The MRM does not explicitly require knowledge of T_{dd} because it was developed to be applicable to radiation fog with a surface-based inversion (Bauer & Howlett, 1995). However, knowledge of the saturation at Z_{base} is necessary to apply this method to fog with a low-level inversion. The comparison between the DDM and the MRM was therefore performed using three T_{dd} thresholds (0.5, 1, and 1.5 °C), and on soundings with at least two saturated sounding levels ($T_{dd} \leq T_{dd}$ threshold) or with one saturated level and a positive dew point temperature gradient immediately above that level. Results for Danmarkshavn are displayed in Figure 8a. There is a systematic tendency of the DDM to lead to higher FTH values compared to the MRM (13- to 20-m higher on average). Even though this difference appears more pronounced at higher T_{dd} thresholds, it is not statistically significant at the 99% confidence level and, moreover, is lower than the vertical accuracy of the calculated geopotential height (25 m). Despite the fact that DDM and MRM give consistent results for vertically extensive fog, it is unsure how accurate either method is for FTH calculation of thin fog ($<$ 100 m agl). Although high-resolution radiosondes can detect shallow fog thicker than 10 m, low-resolution radiosondes have limited capability to detect fog or clouds thinner than a few tens of meters

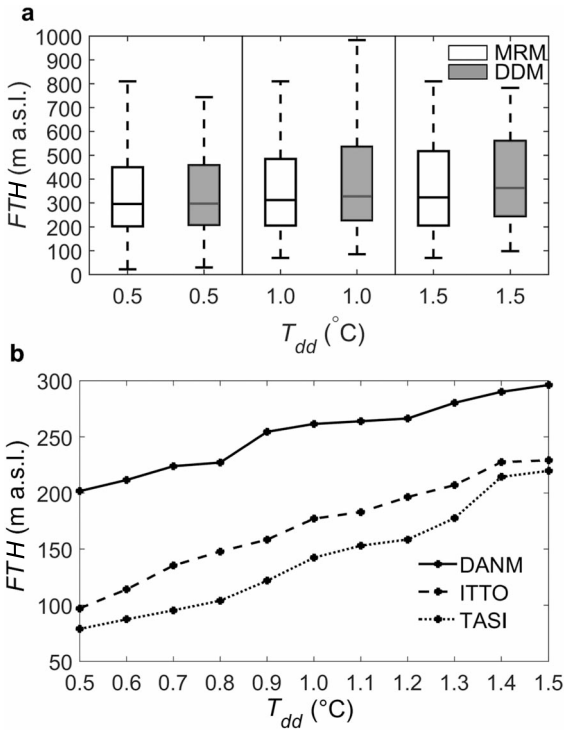

Figure 8. (a) Statistics of fog-top height (FTH) retrieved from IGRA files over Danmarkshavn with the mixing ratio method (MRM, Bauer & Howlett, 1995) and the dew point depression method (DMD, this study) for three dew point depression (T_{dd}) thresholds ($n = 72$). (b) Median FTH over Danmarkshavn (DANM), Ittoqqortoormiit (ITTO), and Tasiilaq (TASI) as a function of T_{dd} threshold (DDM; n = 115, 74, 94). Standard deviations in Figure 8b are 165–734 m, which is on the lower range of standard deviations in Figure 8a.

(Dorman et al., 2017; Zhang et al., 2010). Some thin fog retrieved in this analysis has a thickness < 5 m, which is lower than the accuracy for geopotential height. Moreover, DMI reports invisible sky at the time of these observations, further suggesting an underestimation of the calculated FTH in the case of thin fog.

The sensitivity of the DDM to varying T_{dd} thresholds was analyzed for T_{dd} ranging from 0.5 to 1.5 °C and for soundings with a surface $T_{dds} \leq 0.5$ °C (Figure 8b). Results show that FTH increases with a larger T_{dd} threshold, where differences between medians are 30–80 m when the T_{dd} threshold is changed by only 0.5 °C (which is also the uncertainty in T measurements). The average error induced by the choice of T_{dd} threshold is therefore approximately 50 m. Together with the uncertainty in the calculated geopotential height (25 m), this represents an estimated cumulative error in calculated FTH of $\sqrt{50^2 + 25^2} = 56$ m. The uncertainty linked to the choice of T_{dd} threshold is larger when FTH is lower because shallow fog is usually determined by only one saturated sounding level. Our interpolation algorithm might have limited capability to accurately calculate FTH of shallow fog, particularly fog restricted to the mixed layer, because neglecting hydrostatic balance terms at the local scale can result in the underestimation of FTH. The choice of the T_{dd} threshold, however, does not change the overall conclusions of this study since Danmarkshavn always has the highest FTH values, followed by Ittoqqortoormiit and Tasiilaq (Figure 8b). Nevertheless, the large differences in FTH under a same T_{dd} threshold indicate that the choice of an accurate T_{dd} threshold is the most crucial parameter for precise FTH calculation. Over Arctic locations, we recommend to calibrate T_{dd} threshold relative to surface observations to avoid underestimation (T_{dd} threshold too low) or overestimation of FTH (T_{dd} threshold too high).

5.2. Comparison of FTH With CALIPSO-Derived Cloud Top Height

A total of 149 and 146 CALIPSO tracks were analyzed in the vicinity of Ittoqqortoormiit and Danmarkshavn, respectively, for the melt seasons of 2006–2016. From these, four fog and six low stratus cases were identified for comparison between IGRA and CALIPSO data sets (Table 1). In the very rare cases were Z was reported, it was within 5 m of calculated Z. Four cases (#1, #4, #5, and #8) have cloud top height values within the cumulative error range ($\sqrt{30^2 + 25^2} = 39$ m), or for very thick fog within 10% (#4), and in addition have the same number of cloud layers (good agreement). For cases #2, #3, #6, #7, and #9, both data sets identify the low cloud layer, although CALIPSO reports a cloud top height that is 60–589 m lower. In some cases this may be due to spatial variability in the fog or cloud layers (reasonable agreement). In one case (#10), CALIPSO does not report the lower cloud layer detected by IGRA, which could be attributed to the attenuation of the signal by optically thick clouds aloft (Mace & Zhang, 2014).

Overall, in spite of the spatial and temporal differences between CALIPSO and IGRA, FTH from IGRA via the DDM is in reasonable to good agreement with CALIPSO retrievals for vertically extensive fog and low stratus, under T_{dd} threshold = 1 °C. However, CALIPSO's vertical resolution of 30 m and the considerable distance between the IGRA station and nearest CALIPSO track line points prevent us from reliably verifying the DDM method results for shallow fog ($<$ 100 m agl) or to determine which method (DDM versus MRM) is the most accurate to calculate FTH from radiosondes. Both methods are more suitable over Arctic locations compared to methods using higher T_{dd} thresholds (Poore et al., 1995) or RH thresholds (Wang & Rossow, 1995; Wang et al., 1999; Zhang et al., 2010), and because the DDM and MRM interpolation algorithms are more accurate than using half the distance between saturated and subsaturated sounding levels as the cloud boundary (Wang & Rossow, 1995). Still, we suggest the use of the DDM instead of the MRM because the DDM can be applied to any fog thermodynamic profile.

Table 1
Comparison of CALIPSO and IGRA Low Stratiform Cloud Top Heights Derived Using the DDM

Date[a]	CALIPSO[b] cloud top height (m asl)	IGRA cloud top range from calculated Z[c] (m asl)	IGRA inversion-base height (m asl)	DMI *ww*[d] 11 UTC	DMI *ww*[d] 12 UTC	DMI/IGRA cloud type[e]
Danmarkshavn						
20/05/2016	NA	411–426[f]	411	110	100	Stratus with mist
#1	411[f]					
	352[f]					
	382[f]					
05/08/2009	-	173–180[f]	38	34	30	Fog
#2	113[f]					
	-					
	-					
Ittoqqortoormiit						
03/07/2007	178[f]	737[f]	737	NA	NA	Stratus
#3	148[f]					
	-					
05/07/2008	1,190[g]	1,044–1,095[f]	618	NA	NA	Stratus
#4	1,190[g]					
	2,747[g]					
07/09/2008	1,100[f]	964–1,013[f]	640	NA	NA	Fog
#5	1,071[f]					
	1,131[f]					
12/10/2009	1,160[g]	1,351–1,355[g]	1351	NA	NA	Stratus
#6	1,101[g]					
	1,131[f]					
27/07/2010	232[g]	409–412[f]	351	NA	0	Stratus
#7	262[f]					
	-					
27/05/2011	352[f]	449–471[f]	449	80	0	Stratus
#8	382[f]					
	412[f]					
31/08/2011	1,160[g]	1,363[g]	990	34	33	Fog
#9	1,190[g]					
	1,190[g]					
20/04/2015	4,663[f]	454–457[g]	395	110	131	Stratus and fog
#10	4,693[f]					
	4,693[f]					

Note. NA is no data; - is no cloud top height detected. IGRA = Integrated Global Radiosonde Archive; CALIPSO = Cloud-Aerosol Lidar and Infrared Pathfinder Satellite Observation; DMI = Danish Meteorological Institute.
[a]Observation time IGRA 1200 UTC; CALIPSO 1230 UTC (Danmarkshavn) or 1330 UTC (Ittoqqortoormiit). [b]CALIPSO data retrieved from three or four grid points (Figure 3). [c]Z is the geopotential height. [d]*ww* is the present weather code. [e]Cloud type from DMI (surface) and IGRA profiles (aloft). [f]One cloud layer. [g]Two cloud layers.

5.3. Temperature Inversion Characteristics Comparison and Interpretation

5.3.1. All-Weather Conditions

Results from this study show that temperature inversions are frequent (> 85%) and mostly elevated over east Greenland during the melt season. Overall, the frequency of temperature inversions over east Greenland compares well with values reported with similar melt season low-resolution radiosonde observations over the Arctic Ocean and the Russian Arctic (> 85%, Kahl et al., 1996; Serreze et al., 1992) but is generally higher than over Arctic coastal sites in Canada, Eurasia, and Alaska, where inversions occur in >60% of soundings (Kahl, 1990; Kahl et al., 1992; Serreze et al., 1992). The inversion frequency reported over Tasiilaq is the same as obtained by Mernild and Liston (2010) from field measurements over summers 2005–2006 in front of a valley glacier within 25 km of that station. These comparisons suggest that post-1980 IGRA sounding significant levels are able to capture the frequency of low-tropospheric temperature inversions at Tasiilaq.

IGRA data display an increase in vertical resolution through time because major instrument changes affect the number of significant levels (Antikainen et al., 2002; Durre & Yin, 2008). While only the post-1992 period is considered to be sufficiently accurate for longitudinal analysis of inversions depth over Greenland (Box &

Cohen, 2006; Zhang et al., 2011) found that inversion depth and intensity records are also inhomogeneous within that period. For the IGRA data set in east Greenland we found that the 1980–2016 period is mostly homogeneous in terms of number of levels, and excluding the 1980–1992 time period from our analysis did not alter the statistical results of the inversion characteristics presented here. We therefore proceed with a comparison of inversion characteristics with other Arctic regions.

Inversion-base altitudes (Z_{base}) over east Greenland are within the lower range of values reported over Alaskan sites (50–300 m agl, Kahl, 1990) but are much lower than those reported for the Canadian Arctic where the range is 100–400 m agl (Kahl et al., 1992). Inversion-top heights (Z_{top}) are higher than values measured by Mernild and Liston (2010) near Tasiilaq (500 versus 300 m asl), even when comparing the same years, suggesting either spatial variability or a limited vertical resolution of IGRA profiles. Similar to what Zhang et al. (2011) found for annual surface-based inversions, inversion depths (ΔZ) for all summer inversions are lower over southeast Greenland compared to northeast Greenland. Contrary to the hypothesis of Kahl et al. (1992), cloud cover fraction does not impact ΔZ in coastal east Greenland. ΔZ values are similar to those measured over the Arctic Ocean (150–350 m, Sotiropoulou et al., 2016) but are shallower than over Eurasian/Russian (250–350 m, Serreze et al., 1992), Alaskan (300–500 m, Kahl, 1990), and most of the Canadian Arctic sites (200–500 m, Kahl et al., 1992). Danmarkshavn has stronger inversions than Tasiilaq, which is consistent with results obtained by Zhang et al. (2011) over east Greenland for surface-based inversions. In addition, we highlight that Ittoqqortoormiit is characterized by even stronger inversions, which may be due to the proximity of the cold waters of the Scoresby Sund (Sandell & Sandell, 1991). Inversion intensities (ΔT) over east Greenland are similar to those reported in Arctic Canada (1–3 °C, Kahl et al., 1992) and the Eurasian-Russian coastal Arctic regions (2–3 °C, Serreze et al., 1992) but in the lower range of values measured over the Arctic Ocean (2–4 °C, Sotiropoulou et al., 2016). Inversions are 2–3 times weaker than over Alaskan Arctic sites (4–7 °C, Kahl, 1990).

5.3.2. Fog Conditions

Fog over east Greenland is commonly 200-m thick, which is comparable to geometrical thicknesses reported for Arctic advection fog over the pack ice (Sotiropoulou et al., 2014, 2016; Tjernström et al., 2015) and Antarctic coastal advection fog (Gajananda et al., 2007). Extreme fog events can reach an altitude of 700 m asl, which is comparable to cases of midlatitude marine fog (Gao et al., 2007; Huang et al., 2015; Liu et al., 2016). At higher latitudes and during the late melt season, fog over east Greenland frequently resides inside the inversion layer. This corroborates observations of fog originating from warm and moist advection over melting ice surfaces (Sedlar et al., 2012; Sotiropoulou et al., 2016).

The presence of both fog and higher clouds tends to be associated with an elevated Z_{base}. However, fog and clouds have a contrasting effect on ΔT: while clouds generally weaken the inversion due to increased downward longwave radiation (Kahl, 1990), fog is associated with stronger inversions compared to nonfog conditions. Median ΔT is similar whether fog is below, capped or inside the inversion layer (not shown), suggesting an environmental control on lower-tropospheric stability conditions, which in turn favors fog formation. Fog tends to be associated with more stable conditions because inversions efficiently trap moisture (e.g., Miller et al., 2013). High ΔT during fog can also in part be due to low wind speeds, which are associated with stronger inversions (Figure 6f). Similarly, the deeper inversions encountered during fog could be the result of calm conditions that allow the inversion to develop and settle.

The apparent latitudinal gradient in ΔT during fog conditions can be due to local- and regional-scale environmental factors promoting fog formation. The weather in northern Greenland is dominated by a presence of year-round sea ice, resulting in the persistence of fog and low-level clouds (Cappelen, 2015). Danmarkshavn is therefore under the influence of distinctly different local boundary layer processes compared to the other two stations. The strong thermal gradient between the cold ocean and a warmer land surface creates stronger and more frequent sea breezes associated with fog at Danmarkshavn (Gilson, 2018), which result in fog occurring throughout the day. At Tasiilaq fog is mostly restricted to morning hours (Gueye, 2014). Summer fog in east Greenland is almost always associated with sea breezes, which are mostly easterly surface wind directions at Danmarkshavn, southerly at Tasiilaq, and southwesterly at Ittoqqotoormiit (Gilson, 2018). At the last station, fog originates from the Scoresby Sund fjord instead of the open ocean. Gilson et al. (2018) found that east Greenland fog is generally associated with anticyclonic conditions and that the most frequent vertically extensive fog at Danmarkshavn is associated with veering winds and the blocking of oceanic flow by a high-pressure system over the ice sheet. The presence of a high-pressure ridge over

northeast and central Greenland contributes to establishing strong capping inversions by subsidence processes (Ohmura & Reeh, 1991; Steffen & Box, 2001), which, in combination with strong sea breezes, promotes the occurrence of fog (Koshiro & Shiotani, 2014; Miller et al., 2013). Finally, the lack of influence of cloud cover on ΔT over Danmarkshavn compared to the southern stations could be due to regional differences in cloud properties (e.g., Van Tricht et al., 2016).

6. Summary and Conclusions

Based on the combined analysis of surface synoptic weather data and twice-daily upper-air observations from the IGRA, we presented melt-season inversion characteristics under fog, nonfog, and all-weather conditions at three east Greenland coastal sites over the period 1980–2016. In addition, a novel and robust automated method, the DDM, was introduced and tested. It allows for the retrieval of predominantly liquid or supercooled fog geometrical thickness from low-resolution IGRA radiosondes over any Arctic location.

Temperature inversions occur in >85% of east Greenland summer soundings and are generally elevated (150 m asl) with a median inversion depth of 240 m and an inversion intensity of 2 °C. Retrieved FTH is commonly 150–200 m asl but can reach an altitude of 700 m asl. Fog frequently penetrates the elevated inversion layer over coastal regions during the late melt season (see also Gilson et al., 2018). Compared to nonfog conditions, fog occurs during stronger and deeper inversions. Low wind speed could in part explain these differences. At higher latitudes, fog is thicker and inversions are stronger during fog than during clear-sky or cloudy conditions. We postulate that these regional differences are due to a combination of distinctly different boundary layer and large-scale processes favoring fog formation.

FTH calculated with the DDM from IGRA and retrieved from CALIPSO cloud top product is in reasonable agreement. These results suggest that FTH for vertically extensive fog (> 100 m) can be estimated reliably by the DDM with a dew point depression threshold of 1 °C from IGRA's low-resolution soundings. However, changing this threshold by only 0.5 °C changes the median FTH by 30 to 80 m, leading to a cumulative error of 56 m due to the choice of dew point depression threshold. Despite these uncertainties, the DDM is more suitable to retrieve FTH over Arctic locations compared to current fog and cloud detection methods from low-resolution radiosondes (Bauer & Howlett, 1995; Poore et al., 1995; Wang & Rossow, 1995; Wang et al., 1999).

The sensitivity of radiosonde sensors, and measurement practices and conditions at a station can impact measured dew point depression during fog. The strength of the DDM introduced here is the required calibration of a dew point depression threshold using local WMO station surface observations, making it applicable to any remote coastal Arctic (or Antarctic) WMO location where present weather, visibility, and upper-air measurements exist together. The DDM can additionally be used to detect cloud base and top height from other Arctic boundary layer clouds, such as the more common stratocumulus clouds. In conjunction with the analysis of temperature inversion characteristics, the retrieved geometrical cloud thickness would then allow for quantification of the relationship between all Arctic low-level clouds and temperature inversions. These results will contribute to a deeper understanding of low-level liquid-bearing Arctic stratiform cloud macrophysics and, together with detailed inversion characteristics, will serve in improving Arctic surface energy balance, ice sheet, and regional atmospheric climate models (e.g., Marshall et al., 2007; Van Tricht et al., 2016; van Wessem et al., 2018).

Acknowledgments
We acknowledge funding from the Natural Sciences and Engineering Research Council of Canada, Alberta Innovates Technology Futures, and the University of Lethbridge. The National Oceanic and Atmospheric Administration (NOAA) is thanked for access to the IGRA data. We thank the Danish Meteorological Institute for East Greenland synoptic weather data and the National Aeronautics and Space Administration for making available the CALIPSO data products. All the data used are listed in the references. A Matlab script to extract IGRA data was provided by Andy Rhines (University of Washington) and later adjusted. Scripts used in this paper can be found in Gilson (2018). Matthew Letts, Christopher Hopkinson, Larry Flanagan (University of Lethbridge), Andy Bush (University of Alberta), Ismail Gultepe (Environment Canada), and three anonymous reviewers, are acknowledged for their critical feedback.

References

Alt, B. T. (1979). Investigation of summer synoptic climate controls on the mass balance of Meighen ice cap. *Atmosphere-Ocean*, *17*(3), 181–199. https://doi.org/10.1080/07055900.1979.9649060

Antikainen, V., Paukkunen, A., & Jauhiainen, H. (2002). *Measurement accuracy and repeatability of Vaisala RS90 radiosonde*, *Vaisala News*, (pp. 159, 11–113). Vantaa, Finland: Vaisala.

AMAP (2017). *Snow, Water, Ice and Permafrost in the Arctic (SWIPA) 2017*. Arctic Monitoring and Assessment Programme (AMAP), 2017, Oslo, Norway.

Bauer, B. J., & Howlett, T. (Eds) (1995). *Aerographer's Mate 1 & C, NAVEDTRA 14010*. Washington, DC: Naval Education and Training Professional Development and Technology Center. https://www.weather.gov/media/zhu/ZHU_Training_Page/Met_Tutorials/Met_Tutorial.pdf

Bennartz, R., Shupe, M. D., Turner, D. D., Walden, V. P., Steffen, K., Cox, C. J., et al. (2013). July 2012 Greenland melt extent enhanced by low-level liquid clouds. *Nature*, *496*(7443), 83–86. https://doi.org/10.1038/nature12002

Bintanja, R., Graversen, R. G., & Hazeleger, W. (2011). Arctic winter warming amplified by the thermal inversion and consequent low infrared cooling to space. *Nature Geoscience*, *4*(11), 758–761. https://doi.org/10.1038/ngeo1285

Bintanja, R., & Krikken, F. (2016). Magnitude and pattern of Arctic warming governed by the seasonality of radiative forcing. *Scientific Reports*, *6*(1), 38287. https://doi.org/10.1038/srep38287

Bødtker, E. (2003). *Observation systems 2003*, *Technical Report 03–16*, (p. 10). Copenhagen, Denmark: Ministry of Transport, Danish Meteorological Institute.

Bourne, S. M., Bhatt, U. S., Zhang, J., & Thoman, R. (2010). Surface-based temperature inversions in Alaska from a climate perspective. *Atmospheric Research*, *95*(2-3), 353–366. https://doi.org/10.1016/j.atmosres.2009.09.013

Box, J. E., & Cohen, A. E. (2006). Upper-air temperatures around Greenland: 1964–2005. *Geophysical Research Letters*, *33*, L12706. https://doi.org/10.1029/2006GL025723

Bradley, R. S., Keimig, F. T., & Diaz, H. F. (1992). Climatology of surface-based inversions in the North American Arctic. *Journal of Geophysical Research*, *97*(D14), 15,699–15,712. https://doi.org/10.1029/92JD01451

Busch, N., Ebel, U., Kraus, H., & Schaller, E. (1982). The structure of the subpolar inversion-capped ABL. *Meteorology and Atmospheric Physics*, *31*(1), 1–18. https://doi.org/10.1007/BF02257738

Cappelen, J. (2015). *Greenland - DMI historical climate data collection 1784–2014*, *Technical Report 15–04*, (p. 97). Copenhagen, Denmark: Danish Meteorological Institute.

Cappelen, J., Jørgensen, B. V., & Laursen, E. V. (2001). *The observed climate of Greenland, 1958–99-with climatological standard normals, 1961–90*, *Technical Report 00–18*, (p. 149). Copenhagen, Denmark: Danish Meteorological Institute.

Cermak, J. (2016). Fog frequency and properties from active-sensor satellite data. Paper presented at AGU Fall General Assembly 2016, San Francisco, CA: American Geophysical Union, Abstract id. A21L-07.

Chernykh, I. V., & Eskridge, R. E. (1996). Determination of cloud amount and level from radiosonde soundings. *Journal of Applied Meteorology*, *35*(8), 1362–1369. https://doi.org/10.1175/1520-0450(1996)035<1362:DOCAAL>2.0.CO;2

Chutko, K. J., & Lamoureux, S. F. (2009). The influence of low-level thermal inversions on estimated melt-season characteristics in the central Canadian Arctic. *International Journal of Climatology*, *29*(2), 259–268. https://doi.org/10.1002/joc.1722

Circumpolar Arctic Vegetation Map (2003). Conservation of Arctic flora and fauna (Map 1, scale: 1:7,500,000). Retrieved from [http://www.geobotany.uaf.edu/cavm/]. Anchorage, AK: U.S. Fish and Wildlife Service

Croft, P. J., Pfost, R. L., Medlin, J. M., & Johnson, G. A. (1997). Fog forecasting for the southern region: A conceptual model approach. *Weather and Forecasting*, *12*(3), 545–556. https://doi.org/10.1175/1520-0434(1997)012<0545:FFFTSR>2.0.CO;2

Curry, J. A., Hobbs, P. V., King, M. D., Randall, D. A., Minnis, P., Isaac, G. A., et al. (2000). FIRE Arctic clouds experiment. *Bulletin of the American Meteorological Society*, *81*(1), 5–29. https://doi.org/10.1175/1520-0477(2000)081<0005:FACE>2.3.CO;2

Devasthale, A., Willén, U., Karlsson, K.-G., & Jones, C. G. (2010). Quantifying the clear-sky temperature inversion frequency and strength over the Arctic Ocean during summer and winter seasons from AIRS profiles. *Atmospheric Chemistry and Physics*, *10*(12), 5565–5572. https://doi.org/10.5194/acp-10-5565-2010

Dorman, C. E., Mejia, J., Koračin, D., & McEvoy, D. (2017). Worldwide marine fog occurrence and climatology. In D. Koračin, & C. E. Dorman (Eds.), *Marine fog: Challenges and advancements in observations, modeling, and forecasting*, (pp. 7–152). Cham, Switzerland: Springer International Publishing. https://doi.org/10.1007/978-3-319-45229-6_2

Durre, I., Vose, R. S., & Wuertz, D. B. (2006). Overview of the Integrated Global Radiosonde Archive. *Journal of Climate*, *19*(1), 53–68. https://doi.org/10.1175/JCLI3594.1

Durre, I., & Yin, X. (2008). Enhanced radiosonde data for studies of vertical structure. *Bulletin of the American Meteorological Society*, *89*(9), 1257–1262. https://doi.org/10.1175/2008BAMS2603.1

Eastman, R., & Warren, S. G. (2010). Arctic cloud changes from surface and satellite observations. *Journal of Climate*, *23*(15), 4233–4242. https://doi.org/10.1175/2010JCLI3544.1

Flato, G., Marotzke, J., Abiodun, B., Braconnot, P., Chou, S. C., Collins, W., et al. (2013). Evaluation of climate models. In T. F. Stocker, D. Qin, G.-K. Plattner, M. Tignor, S. K. Allen, J. Boschung, et al. (Eds.), *Climate Change 2013: The Physical Science Basis. Contribution of Working Group I to the Fifth Assessment Report of the Intergovernmental Panel on Climate Change*, (pp. 741–866). Cambridge, United Kingdom and New York, NY: Cambridge University Press.

Fochesatto, G. J. (2015). Methodology for determining multilayered temperature inversions. *Atmospheric Measurement Techniques*, *8*(5), 2051–2060. https://doi.org/10.5194/amt-8-2051-2015

Ford, J. D., & Furgal, C. (2009). Foreword to the special issue: Climate change impacts, adaptation and vulnerability in the Arctic. *Polar Research*, *28*(1), 1–9. https://doi.org/10.1111/j.1751-8369.2009.00103.x

Gajananda, K., Dutta, H. N., & Lagun, V. E. (2007). An episode of coastal advection fog over east Antarctica. *Current Science*, *93*(5), 654–659.

Gao, S., Lin, H., Shen, B., & Fu, G. (2007). A heavy sea fog event over the Yellow Sea in March 2005: Analysis and numerical modeling. *Advances in Atmospheric Sciences*, *24*(1), 65–81. https://doi.org/10.1007/s00376-007-0065-2

Gilson, G. F. (2018). Macrophysical properties and a climatology of Arctic coastal fog in east Greenland, (Doctoral Dissertation). Retrieved from OPUS database (https://www.uleth.ca/dspace/handle/10133/5038). Lethbridge, AB, Canada: University of Lethbridge.

Gilson, G. F., Jiskoot, H., Cassano, J. J., Gultepe, I., & James, T. D. (2018). The thermodynamic structure of Arctic coastal fog occurring during the melt season over east Greenland. *Boundary-Layer Meteorology*, *168*(3), 443–467. https://doi.org/10.1007/s10546-018-0357-3

Gueye, S. (2014). Frequency, timing and temporal patterns of regional coastal Arctic fog in east Greenland. (Master's thesis). Retrieved from FNWI (Science) Education Service Centre (https://esc.fnwi.uva.nl/thesis/centraal/files/f1561562580.pdf). Amsterdam, Netherlands: University of Amsterdam.

Haimberger, L. (2007). Homogenization of radiosonde temperature time series using innovation statistics. *Journal of Climate*, *20*(7), 1377–1403. https://doi.org/10.1175/JCLI4050.1

Hanesiak, J. M., & Wang, X. L. (2005). Adverse-weather trends in the Canadian Arctic. *Journal of Climate*, *18*(16), 3140–3156. https://doi.org/10.1175/JCLI3505.1

Hanna, E., & Cappelen, J. (2003). Recent cooling in coastal southern Greenland and relation with the North Atlantic Oscillation. *Geophysical Research Letters*, *30*(3), 1132. https://doi.org/10.1029/2002GL015797

Hardy, B. (1998). *Determination of relative humidity in subzero temperatures*, *RH System*, (p. 5). Albuquerque, NM: World Meteorological Organization.

Hofer, S., Tedstone, A. J., Fettweis, X., & Bamber, J. L. (2017). Decreasing cloud cover drives the recent mass loss on the Greenland ice sheet. *Science Advances*, *3*(6), e1700584. https://doi.org/10.1126/sciadv.1700584

Huang, H., Liu, H., Huang, J., Mao, W., & Bi, X. (2015). Atmospheric boundary layer structure and turbulence during sea fog on the southern China coast. *Monthly Weather Review*, *143*(5), 1907–1923. https://doi.org/10.1175/MWR-D-14-00207.1

Hudson, S. R., & Brandt, R. E. (2005). A look at the surface-based temperature inversion on the Antarctic plateau. *Journal of Climate*, *18*(11), 1673–1696. https://doi.org/10.1175/JCLI3360.1

Intergovernmental Panel on Climate Change (2013). Summary for policymakers. In T. F. Stocker, D. Qin, G.-K. Plattner, M. Tignor, S. K. Allen, J. Boschung, et al. (Eds.), *Climate Change 2013: The Physical Science Basis. Contribution of Working Group I to the Fifth Assessment Report of the Intergovernmental Panel on Climate Change*, (pp. 1–30). Cambridge, United Kingdom and New York, NY: Cambridge University Press.

Jin, X., Hanesiak, J., & Barber, D. (2007). Detecting cloud vertical structures from radiosondes and MODIS over Arctic first-year sea ice. *Atmospheric Research*, *83*(1), 64–76. https://doi.org/10.1016/j.atmosres.2006.03.003

Kahl, J. D. (1990). Characteristics of the low-level temperature inversion along the Alaskan Arctic coast. *International Journal of Climatology*, *10*(5), 537–548. https://doi.org/10.1002/joc.3370100509

Kahl, J. D., Martinez, D. A., & Zaitseva, N. A. (1996). Long-term variability in the low-level inversion layer over the Arctic Ocean. *International Journal of Climatology*, *16*(11), 1297–1313. https://doi.org/10.1002/(SICI)1097-0088(199611)16:11<1297::AID-JOC86>3.0.CO;2-T

Kahl, J. D., Serreze, M. C., & Schnell, R. C. (1992). Tropospheric low-level temperature inversions in the Canadian Arctic. *Atmosphere-Ocean*, *30*(4), 511–529. https://doi.org/10.1080/07055900.1992.9649453

Kattsov, V. M., & Källén, E. (2005). Future climate change: Modeling and scenarios for the Arctic. In C. Symon, L. Arris, & B. Heal (Eds.), *Arctic Climate Impact Assessment*, (pp. 99–150). Cambridge, United Kingdom and New York, NY: Cambridge University Press.

Kawai, H., Yabu, S., Hagihara, Y., Koshiro, T., & Okamoto, H. (2015). Characteristics of the cloud top heights of marine boundary layer clouds and the frequency of marine fog over mid-latitudes. *Journal of the Meteorological Society of Japan Ser II*, *93*(6), 613–628. https://doi.org/10.2151/jmsj.2015-045

Key, E. L., Minnett, P. J., & Jones, R. A. (2004). Cloud distributions over the coastal Arctic Ocean: Surface-based and satellite observations. *Atmospheric Research*, *72*(1-4), 57–88. https://doi.org/10.1016/j.atmosres.2004.03.029

Kim, C. K., & Yum, S. S. (2010). Local meteorological and synoptic characteristics of fogs formed over Incheon international airport in the west coast of Korea. *Advances in Atmospheric Sciences*, *27*(4), 761–776. https://doi.org/10.1007/s00376-009-9090-7

Klein, S. A., & Hartmann, D. L. (1993). The seasonal cycle of low stratiform clouds. *Journal of Climate*, *6*(8), 1587–1606. https://doi.org/10.1175/1520-0442(1993)006<1587:TSCOLS>2.0.CO;2

Koračin, D., Dorman, C. E., Lewis, J. M., Hudson, J. G., Wilcox, E. M., & Torregrosa, A. (2014). Marine fog: A review. *Atmospheric Research*, *143*, 142–175. https://doi.org/10.1016/j.atmosres.2013.12.012

Koshiro, T., & Shiotani, M. (2014). Relationship between low stratiform cloud amount and estimated inversion strength in the lower troposphere over the global ocean in terms of cloud types. *Journal of the Meteorological Society of Japan Ser II*, *92*(1), 107–120. https://doi.org/10.2151/jmsj.2014-107

Lanzante, J. R. (1996). Resistant, robust and non-parametric techniques for the analysis of climate data: Theory and examples, including applications to historical radiosonde station data. *International Journal of Climatology*, *16*(11), 1197–1226. https://doi.org/10.1002/(SICI)1097-0088(199611)16:11<1197::AID-JOC89>3.0.CO;2-L

Lesins, G., Duck, T. J., & Drummond, J. R. (2012). Surface energy balance framework for Arctic amplification of climate change. *Journal of Climate*, *25*(23), 8277–8288. https://doi.org/10.1175/JCLI-D-11-00711.1

Lewis, J. M., Koračin, D., Rabin, R., & Businger, J. (2003). Sea fog off the California coast: Viewed in the context of transient weather systems. *Journal of Geophysical Research*, *108*(D15), 4457. https://doi.org/10.1029/2002JD002833

Lewis, S. M., & Smith, L. C. (2009). Hydrologic drainage of the Greenland ice sheet. *Hydrological Processes*, *23*(14), 2004–2011. https://doi.org/10.1002/hyp.7343

Liu, D. Y., Yan, W. L., Yang, J., Pu, M. J., Niu, S. J., & Li, Z. H. (2016). A study of the physical processes of an advection fog boundary layer. *Boundary-Layer Meteorology*, *158*(1), 125–138. https://doi.org/10.1007/s10546-015-0076-y

Mace, G. G., & Zhang, Q. (2014). The CloudSat radar-lidar geometrical profile product (RL-GeoProf): Updates, improvements, and selected results. *Journal of Geophysical Research: Atmospheres*, *119*, 9441–9462. https://doi.org/10.1002/2013JD021374

Marshall, S. J., Sharp, M. J., Burgess, D. O., & Anslow, F. S. (2007). Near-surface-temperature lapse rates on the Prince of Wales Icefield, Ellesmere Island, Canada: Implications for regional downscaling of temperature. *International Journal of Climatology*, *27*(3), 385–398. https://doi.org/10.1002/joc.1396

Mauritsen, T., Sedlar, J., Tjernström, M., Leck, C., Martin, M., Shupe, M., et al. (2011). An Arctic CCN-limited cloud-aerosol regime. *Atmospheric Chemistry and Physics*, *11*(1), 65–173. https://doi.org/10.5194/acp-11-165-2011

Mernild, S. H., Hansen, B. U., Jakobsen, B. H., & Hasholt, B. (2008). Climatic conditions at the Mittivakkat glacier catchment (1994–2006), Ammassalik Island, SE Greenland, and in a 109-year perspective (1898–2006). *Geografisk Tidsskrift-Danish Journal of Geography*, *108*(1), 51–72. https://doi.org/10.1080/00167223.2008.10649574

Mernild, S. H., & Liston, G. E. (2010). The influence of air temperature inversions on snowmelt and glacier mass balance simulations, Ammassalik Island, Southeast Greenland. *Journal of Applied Meteorology and Climatology*, *49*(1), 47–67. https://doi.org/10.1175/2009JAMC2065.1

Meyer, W. D., & Rao, G. V. (1999). Radiation fog prediction using a simple numerical model. *Pure and Applied Geophysics*, *155*(1), 57–80. https://doi.org/10.1007/s000240050254

Miller, N. B., Shupe, M. D., Cox, C. J., Walden, V. P., Turner, D. D., & Steffen, K. (2015). Cloud radiative forcing at Summit, Greenland. *Journal of Climate*, *28*(15), 6267–6280. https://doi.org/10.1175/JCLI-D-15-0076.1

Miller, N. B., Turner, D. D., Bennartz, R., Shupe, M. D., Kulie, M. S., Cadeddu, M. P., & Walden, V. P. (2013). Surface-based inversions above central Greenland. *Journal of Geophysical Research: Atmospheres*, *118*, 495–506. https://doi.org/10.1029/2012JD018867

Minnis, P., Yi, Y., Huang, J., & Ayers, K. (2005). Relationships between radiosonde and RUC-2 meteorological conditions and cloud occurrence determined from ARM data. *Journal of Geophysical Research*, *110*, D23204. https://doi.org/10.1029/2005JD006005

Nardino, M., & Georgiadis, T. (2003). Cloud type and cloud cover effects on the surface radiative balance at several polar sites. *Theoretical and Applied Climatology*, *74*(3–4), 203–215. https://doi.org/10.1007/s00704-002-0708-2

National Oceanic and Atmospheric Administration (1995). Surface weather observations and reports (Federal Meteorological Handbook No. 1, 94 pp.). Washington, DC: US Department of Commerce, National Oceanic and Atmospheric Administration.

Nilsson, E. D., & Bigg, E. K. (1996). Influences on formation and dissipation of high Arctic fogs during summer and autumn and their interaction with aerosol. *Tellus Series B: Chemical and Physical Meteorology*, *48*(2), 234–253. https://doi.org/10.3402/tellusb.v48i2.15889

Nygård, T., Valkonen, T., & Vihma, T. (2014). Characteristics of Arctic low-tropospheric humidity inversions based on radio soundings. *Atmospheric Chemistry and Physics*, *14*(4), 1959–1971. https://doi.org/10.5194/acp-14-1959-2014

Ohmura, A., & Reeh, N. (1991). New precipitation and accumulation maps for Greenland. *Journal of Glaciology*, *37*(125), 140–148. https://doi.org/10.1017/S0022143000042891

Oke, T. R. (Ed) (1987). *Boundary layer climates*, (2nd ed.). London, UK: Methuen & Co. Ltd.

Palarz, A., Celiński-Mysław, D., & Ustrnul, Z. (2018). Temporal and spatial variability of surface-based inversions over Europe based on ERA-Interim reanalysis. *International Journal of Climatology*, *38*(1), 158–168. https://doi.org/10.1002/joc.5167

Petterssen, S. (Ed) (1956). *Weather analysis and forecasting*, (2nd ed., Vol. 2). New York, NY: McGraw-Hill Publ. Inc.

Pfeffer, W. T., Arendt, A. A., Bliss, A., Bolch, T., Cogley, J. G., Gardner, A. S., et al. (2014). The Randolph Glacier Inventory: A globally complete inventory of glaciers. *Journal of Glaciology*, *60*(221), 537–552. https://doi.org/10.3189/2014JoG13J176

Pithan, F., & Mauritsen, T. (2014). Arctic amplification dominated by temperature feedbacks in contemporary climate models. *Nature Geoscience*, *7*(3), 181–184. https://doi.org/10.1038/ngeo2071

Poore, K. D., Wang, J., & Rossow, W. B. (1995). Cloud layer thicknesses from a combination of surface and upper-air observations. *Journal of Climate*, *8*(3), 550–568. https://doi.org/10.1175/1520-0442(1995)008<0550:CLTFAC>2.0.CO;2

Rae, R. W. (1951). *Climate of the Canadian Arctic Archipelago*. Toronto, ON: Canada Department of Transport, Meteorological Branch.

Román-Cascón, C., Yagüe, C., Steeneveld, G.-Y., Sastre, M., Arrillaga, J. A., & Maqueda, G. (2015). Estimating fog-top height through near-surface micrometeorological measurements. *Atmospheric Research*, *170*, 76–86. https://doi.org/10.1016/j.atmosres.2015.11.016

Sandell, H. T., & Sandell, B. (Eds) (1991). *Archaeology and environment in the Scoresby Sund fjord: Ethno-archaeological investigations of the last Thule culture of northeast Greenland. Meddelelser om Grønland, Man & Society, 1991–15*. Copenhagen, Denmark: Museum Tusculanum Press.

Screen, J. A., & Simmonds, I. (2010). The central role of diminishing sea ice in recent Arctic temperature amplification. *Nature*, *464*(7293), 1334–1337. https://doi.org/10.1038/nature09051

Sedlar, J., Shupe, M. D., & Tjernström, M. (2012). On the relationship between thermodynamic structure and cloud top, and its climate significance in the Arctic. *Journal of Climate*, *25*(7), 2374–2393. https://doi.org/10.1175/JCLI-D-11-00186.1

Sedlar, J., & Tjernström, M. (2009). Stratiform cloud—Inversion characterization during the Arctic melt season. *Boundary-Layer Meteorology*, *132*(3), 455–474. https://doi.org/10.1007/s10546-009-9407-1

Serreze, M. C., & Barry, R. G. (2011). Processes and impacts of Arctic amplification: A research synthesis. *Global and Planetary Change*, *77*(1–2), 85–96. https://doi.org/10.1016/j.gloplacha.2011.03.004

Serreze, M. C., & Francis, J. A. (2006). The Arctic amplification debate. *Climatic Change*, *76*(3–4), 241–264. https://doi.org/10.1007/s10584-005-9017-y

Serreze, M. C., Holland, M. M., & Stroeve, J. (2007). Perspectives on the Arctic's shrinking sea-ice cover. *Science*, *315*(5818), 1533–1536. https://doi.org/10.1126/science.1139426

Serreze, M. C., Schnell, R. C., & Kahl, J. D. (1992). Low-level temperature inversions of the Eurasian Arctic and comparisons with Soviet drifting station data. *Journal of Climate*, *5*(6), 615–629. https://doi.org/10.1175/1520-0442(1992)005<0615:LLTIOT>2.0.CO;2

Shupe, M. D., & Intrieri, J. M. (2004). Cloud radiative forcing of the Arctic surface: The influence of cloud properties, surface albedo, and solar zenith angle. *Journal of Climate*, *17*(3), 616–628. https://doi.org/10.1175/1520-0442(2004)017<0616:CRFOTA>2.0.CO;2

Shupe, M. D., Persson, P. O. G., Brooks, I. M., Tjernström, M., Sedlar, J., Mauritsen, T., et al. (2013). Cloud and boundary layer interactions over the Arctic sea ice in late summer. *Atmospheric Chemistry and Physics*, *13*(18), 9379–9399. https://doi.org/10.5194/acp-13-9379-2013

Sotiropoulou, G., Sedlar, J., Tjernström, M., Shupe, M. D., Brooks, I. M., & Persson, P. O. G. (2014). The thermodynamic structure of summer Arctic stratocumulus and the dynamic coupling to the surface. *Atmospheric Chemistry and Physics*, *14*(22), 12,573–12,592. https://doi.org/10.5194/acp-14-12573-2014

Sotiropoulou, G., Tjernström, M., Sedlar, J., Achtert, P., Brooks, B. J., Brooks, I. M., et al. (2016). Atmospheric conditions during the Arctic Clouds in Summer Experiment (ACSE): Contrasting open water and sea ice surfaces during melt and freeze-up seasons. *Journal of Climate*, *29*(24), 8721–8744. https://doi.org/10.1175/JCLI-D-16-0211.1

Steffen, K., & Box, J. (2001). Surface climatology of the Greenland ice sheet: Greenland climate network 1995–1999. *Journal of Geophysical Research*, *106*(D24), 33,951–33,964. https://doi.org/10.1029/2001JD900161. https://doi.org/10.1029/2001JD900161

Svendsen, H., Beszczynska-Møller, A., Hagen, J. O., Lefauconnier, B., Tverberg, V., Gerland, S., et al. (2002). The physical environment of Kongsfjorden–Krossfjorden, an Arctic fjord system in Svalbard. *Polar Research*, *21*(1), 133–166. https://doi.org/10.1111/j.1751-8369.2002.tb00072.x

Taylor, P. C., Cai, M., Hu, A. X., Meehl, J., Washington, W., & Zhang, G. J. (2013). A decomposition of feedback contributions to polar warming amplification. *Journal of Climate*, *26*(18), 7023–7043. https://doi.org/10.1175/JCLI-D-12-00696.1

Tjernström, M., Shupe, M. D., Brooks, I. M., Persson, P. O. G., Prytherch, J., Salisbury, D. J., et al. (2015). Warm-air advection, air mass transformation and fog causes rapid ice melt. *Geophysical Research Letters*, *42*(13), 5594–5602. https://doi.org/10.1002/2015GL064373

Vaisala (2017) Radiosonde RS92: http://www.vaisala.com/en/products-/soundingsystemsandradiosondes/radiosondes/Pages/RS92.aspx (accessed on 28 May, 2017).

Van Tricht, K., Lhermitte, S., Lenaerts, J. T., Gorodetskaya, I. V., L'Ecuyer, T. S., Noël, B., et al. (2016). Clouds enhance Greenland ice sheet meltwater runoff. *Nature Communications*, *7*(10266). https://doi.org/10.1038/ncomms10266

van Wessem, J. M., van de Berg, W. J., Noël, B. P. Y., van Meijgaard, E., Birnbaum, G., Jakobs, C. L., et al. (2018). Modelling the climate and surface mass balance of polar ice sheets using RACMO2, part 2: Antarctica (1979–2016). *The Cryosphere Discussions*, *12*, 1643–1649. https://doi.org/10.5194/tc-2017-202

Vinje, T. (2001). Fram Strait ice fluxes and atmospheric circulation: 1950–2000. *Journal of Climate*, *14*(16), 3508–3517. https://doi.org/10.1175/1520-0442(2001)014<3508:FSIFAA>2.0.CO;2

Wang, J., & Rossow, W. B. (1995). Determination of cloud vertical structure from upper-air observations. *Journal of Applied Meteorology*, *34*(10), 2243–2258. https://doi.org/10.1175/1520-0450(1995)034<2243:DOCVSF>2.0.CO;2

Wang, J., Rossow, W. B., Uttal, T., & Rozendaal, M. (1999). Variability of cloud vertical structure during ASTEX observed from a combination of rawinsonde, radar, ceilometer and satellite. *Monthly Weather Review*, *127*(10), 2484–2502. https://doi.org/10.1175/1520-0493(1999)127<2484:VOCVSD>2.0.CO;2

Wang, W., Zender, C. S., van As, D., Smeets, P., & van den Broeke, M. R. (2016). Cloud-induced stabilization of Greenland surface melt. Paper presented at AGU Fall General Assembly 2016, American Geophysical Union, San Francisco, CA, Abstract id. A23M-08.

Winker, D. M., Vaughan, M. A., Omar, A., Hu, Y., Powell, K. A., Liu, Z., et al. (2009). Overview of the CALIPSO mission and CALIOP data processing algorithms. *Journal of Atmospheric and Oceanic Technology*, *26*(11), 2310–2323. https://doi.org/10.1175/2009JTECHA1281.1

World Meteorological Organization (1995). Manual on codes, Volume I.1: Part a – Alphanumeric Codes (WMO-No. 306, 503 pp). Geneva, Switzerland.

Zhang, J., Chen, H., Li, Z., Fan, X., Peng, L., Yu, Y., & Cribb, M. (2010). Analysis of cloud layer structure in Shouxian, China using RS92 radiosonde aided by 95 GHz cloud radar. *Journal of Geophysical Research*, *115*, D00K10. https://doi.org/10.1029/2010JD014030

Zhang, J., Li, Z., Chen, H., & Cribb, M. (2013). Validation of a radiosonde-based cloud layer detection method against a ground-based remote sensing method at multiple ARM sites. *Journal of Geophysical Research: Atmospheres*, *118*, 846–858. https://doi.org/10.1029/2012JD018515

Zhang, Y., Seidel, D. J., Golaz, J. C., Deser, C., & Tomas, R. A. (2011). Climatological characteristics of Arctic and Antarctic surface-based inversions. *Journal of Climate*, *24*(19), 5167–5186. https://doi.org/10.1175/2011JCLI4004.1

Zhang, Y. H., & Seidel, D. J. (2011). Challenges in estimating trends in Arctic surface-based inversions from radiosonde data. *Geophysical Research Letters*, *38*, L17806. https://doi.org/10.1029/2011GL048728